Tunable dual plasmon-induced transparency based on a monolayer graphene metamaterial and its terahertz sensing performance

JIAHAO GE,[1] CHENGLONG YOU,[2] HE FENG,[1] XIAOMAN LI,[1] MEI WANG,[1] LIFENG DONG,[3] GEORGIOS VERONIS,[4,5] AND MAOJIN YUN[1,*]

[1]*College of Physics, Center for Marine Observation and Communications, Qingdao University, Qingdao 266071, China*

[2]*Hearne Institute for Theoretical Physics and Department of Physics and Astronomy, Louisiana State University, Baton Rouge, Louisiana 70803, USA*

[3]*Department of Physics, Hamline University, St. Paul 55104, USA*

[4]*School of Electrical Engineering and Computer Science, Louisiana State University, Baton Rouge, Louisiana 70803, USA*

[5]*Center for Computation and Technology, Louisiana State University, Baton Rouge, Louisiana 70803, USA*

[*]*mjyun@qdu.edu.cn*

Abstract: In this paper, tunable dual plasmon-induced transparency (PIT) is achieved by using a monolayer graphene metamaterial in the terahertz region, which consists of two graphene strips of different sizes and a graphene ring. As the dual PIT effect is induced by the destructive interference between the two quasi-dark modes and the bright mode, we propose a four-level plasmonic system based on the linearly coupled Lorentzian oscillators to explain the mechanism behind the dual PIT. It is proved that the theoretical results agree well with the simulation results. Most importantly, the sensing properties of the designed device have been investigated in detail and we found that it can exhibit high sensitivities and figure of merit (FOM). Furthermore, the dual PIT windows can be effectively modulated by changing the Fermi energy of the graphene layer and the angle of incidence. Thus, the proposed graphene-based metamaterial can hold wide applications for switches, modulators, and multi-band refractive index sensors in the terahertz region.

1. Introduction

In recent years, metamaterials, a new type of artificial materials consisting of subwavelength unit cells, have engaged many scientists' attention owing to their extraordinary properties which are different from natural materials. Graphene, a two-dimensional form of carbon, has also been investigated quite intensively in recent years [1,2] due to its high carrier mobility [3,4], low transmission loss [5], and electrical tunability [6–8]. Since the Fermi energy can be easily changed through altering the bias voltage [9,10], graphene has greater potential compared to noble metals [11] to lead to tunable plasmon metamaterials. Surface plasmons (SPs), including surface plasmon polaritons (SPPs) and localized surface plasmons (LSPs), are surface electromagnetic waves existing at the interface between a metal and a dielectric [12]. Plasmon-induced transparency (PIT) [13], is a classical plasmonic analog of electromagnetically induced transparency (EIT) [14,15], and does not require rigorous experimental conditions such as gaseous medium, stable optical pumping, and extremely low-temperature environment [16]. In general, single PIT originates from the coupling of a bright and a dark mode [17,18] or two bright modes [19,20]. In other words, the generation of an EIT analog in plasmonic metamaterials can be achieved by two different approaches: bright-dark mode coupling and bright-bright mode coupling [20].

In addition to the single PIT effect, the multispectral PIT effect can also be realized in graphene-based metamaterials. However, in order to realize the multispectral PIT effect, most metamaterials proposed by researchers in recent years are based on multilayer graphene structures [21–24] or hybrid metal-graphene nanostructures [25], which undoubtedly increase the difficulty of manufacturing. A few researchers realized multispectral PIT by using a simple monolayer graphene metamaterial in the terahertz region [26,27].

PIT metamaterials have many other potential applications such as slow-light devices [28,29] and modulators [30,31]. In addition, since the PIT effect with a sharp transparency window has the strong ability to confine electromagnetic fields, another important application of PIT metamaterials is sensing. In general, THz waves can be used to detect biological macromolecules, since organic molecules exhibit strong absorption and dispersion in the THz frequency range when they interact with each other. However, most natural materials lack a strong response THz waves, limiting their sensing capability. Fortunately, graphene can support THz LSPs. The ultrathin thickness of graphene further increases the electromagnetic field confinement capacity of the PIT effect. Thus, many graphene-based PIT metamaterials have been proposed and used for sensing [32,33]. However, most reported sensors cannot meet the requirements of practical applications owing to their low sensitivities. Designing highly sensitive sensors is therefore important for sensing.

Motivated by recent work in this area, in this paper, we propose a monolayer graphene metamaterial, which consists of two graphene strips with different size and a graphene ring, to realize tunable dual PIT in the terahertz range. All components can couple directly with the external field, and the destructive interference between them induces the dual PIT effect. To better understand the principles behind it, we numerically calculate the electric field distributions and propose a simple four-level plasmonic system based on the coupled Lorentzian oscillators. The theoretical results agree well with the finite element method (FEM) simulation results. Under certain conditions, the refractive index sensing properties of two PIT transmission peaks are $S_1 = 0.92$ THz/RIU and $S_2 = 1.08$ THz/RIU, respectively. The influence of the refractive index of the substrate on the sensitivities is also studied in detail. In addition, the dual PIT effect can be effectively modulated by changing the Fermi energy of the graphene layer and the angle of the incident light. Based on the above advantages, the proposed metamaterial can be used not only for sensors but also for optical switches and modulators in the terahertz region.

2. Structure design and methods

As illustrated in Fig. 1(a), the proposed graphene metamaterial is fabricated on top of the silica (SiO$_2$) substrate with a refractive index of 1.5. An ion-gel layer with a refractive index of 1.43 [34] is spin-coated on the graphene patterns, and the gold gate contacts are deposited onto the ion-gel layer. Thus, we can adjust the Fermi energy of the graphene layer by controlling the bias voltage between the gold gate contacts and the substrate [35]. It has been demonstrated that the Fermi energy of graphene can be dynamically tuned from 0.2 eV to 1.2 eV by applying a high bias voltage [36]. Figure 1(b) shows the top view of the unit cell, which consists of two graphene strips with different size and a graphene ring. The ring is tangent to the centers of both the left and right strips. To better distinguish these components, we refer to the graphene ring, the left strip, the right strip, the combination of the left strip and the ring, and the combination of the right strip and the ring as *C*, *LS*, *RS*, *LSC*, and *RSC*, respectively. The geometrical parameters of the unit cell are given in Fig. 1(b) and they will not change throughout the paper unless otherwise indicated. In this study, the transmission spectra and electric field distributions of the proposed metamaterial are calculated using the commercial software COMSOL which is based on the FEM. The terahertz plane wave polarized in the *y* direction propagates in the normal (*z*) direction towards the surface of the structure. Periodic boundary conditions are applied in the *x* and *y* directions, and perfectly matched layer (PML) absorbing boundary conditions are used in the *z*

direction. The computation domain is discretized using a user-controlled inhomogeneous mesh. The maximum element size of the graphene layer is set equal to 0.5µm to ensure the accuracy of the simulation results. The numerical method above has been verified by reproducing the results in Refs. [28,37].
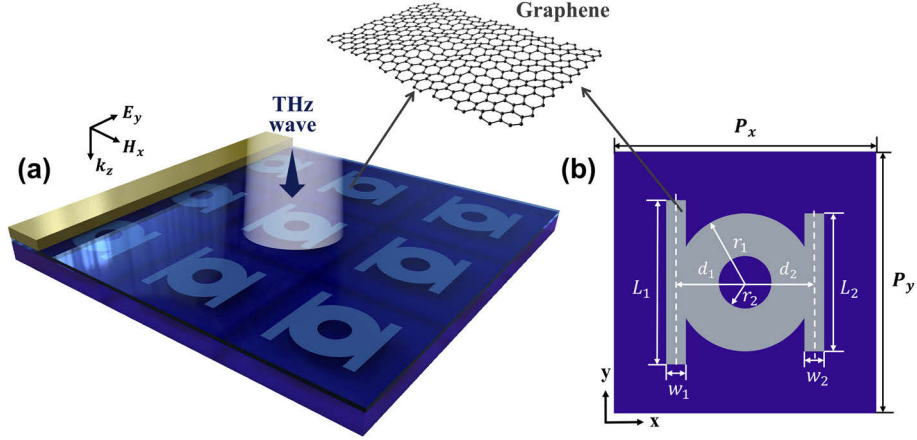
Fig. 1. (a) Schematic diagram of the graphene metamaterial on a dielectric substrate. (b) Top view of the structural unit of the metamaterial. The dimensions are: L_1=12.5µm, L_2=10.5µm, w_1=w_2=1.5µm, r_1=5.25µm, r_2=2µm, d_1=d_2=5.25µm, P_x=P_y=20µm.

Graphene is modeled as a conductive surface by using the transition boundary condition and its thickness is set equal to t_g=1nm [38]. The conductivity of graphene, including interband and intraband contributions, can be obtained from the Kubo formula [39,40]

$$\sigma(\omega) = \frac{2e^2 k_B T}{\pi \hbar^2} \frac{i}{\omega + i\tau^{-1}} \ln\left[2\cosh\left(\frac{E_F}{2k_B T}\right)\right] + \frac{e^2}{4\hbar^2}\left[\frac{1}{2} + \frac{1}{\pi}\arctan\left(\frac{\hbar\omega - 2E_F}{2k_B T}\right)\right]$$
$$- \frac{e^2}{4\hbar}\left[\frac{i}{2\pi}\ln\frac{(\hbar\omega + 2E_F)^2}{(\hbar\omega - 2E_F)^2 + 4(k_B T)^2}\right], \tag{1}$$

where k_B is the Boltzmann constant, e is the electron charge, T = 300K is the temperature, $\hbar$ is the reduced Planck's constant, ω is the angular frequency of the incident light, and E_F is the Fermi energy of graphene. $\tau = \mu E_F / e v_F^2$ is the carrier relaxation lifetime, where $v_F = 1 \times 10^6$ m·s^{-1} denotes the Fermi velocity, and μ_c=10000 cm^2·V^{-1}·S^{-1} represents the carrier mobility. Carrier mobility is an important parameter reflecting the conductivity of graphene. According to previous reports, its highest value for a graphene film on a silica substrate can reach 40000 cm^2·V^{-1}·S^{-1} at room temperature [41]. By considering our device's performance and practical feasibility, we choose 30000 cm^2·V^{-1}·S^{-1} as the value of the carrier mobility. In the terahertz frequency range ($E_F \gg \hbar\omega$), the surface conductivity of graphene can be simplified by neglecting the interband contribution, and the condition $E_F \gg k_B T$ is fulfilled at room temperature. As a result, it can be calculated using [38,39]

$$\sigma(\omega) = \frac{e^2 E_F}{\pi \hbar^2} \frac{i}{\omega + i\tau^{-1}}. \tag{2}$$

The effective permittivity of graphene can then be calculated through $\varepsilon(\omega) = 1 + i\sigma(\omega) / \varepsilon_0 \omega t_g$ [42], where ε_0 is the vacuum dielectric permittivity.

3. Simulation results and theoretical analysis

3.1. Simulation results

The transmission spectra of several different structures are shown in Fig. 2. In Fig. 2(a), we observe that there is coupling between the *LS*, *RS*, and *C* structures and the incident light with resonant dips at 2.39 THz, 2.75 THz, and 3.76 THz, respectively. The measured *Q*-factors for the modes of the *C*, *LS*, and *RS* structures are ~8.3, ~12.6, and ~16.2, respectively. We note that the *Q*-factor can be calculated from $Q = f_0/FWHM$, where f_0 is the resonant frequency and *FWHM* [the pink shade in Fig. 2(a)] is the full width at half maximum bandwidth. Even though these structures can be directly excited by the incident light, the coupling strengths between each of them and the incident light are different. The larger the *Q*-factor, the weaker the coupling strength. Thus, we classify the mode of the *C* structure with the lowest *Q*-factor as a bright mode, and the modes of the *LS* and *RS* structures with larger *Q*-factors as quasi-dark modes [43–45]. Here we would like to emphasize that, although we classify the modes of the *LS* and *RS* structures as quasi-dark modes, these modes do couple to the incident light. They are therefore
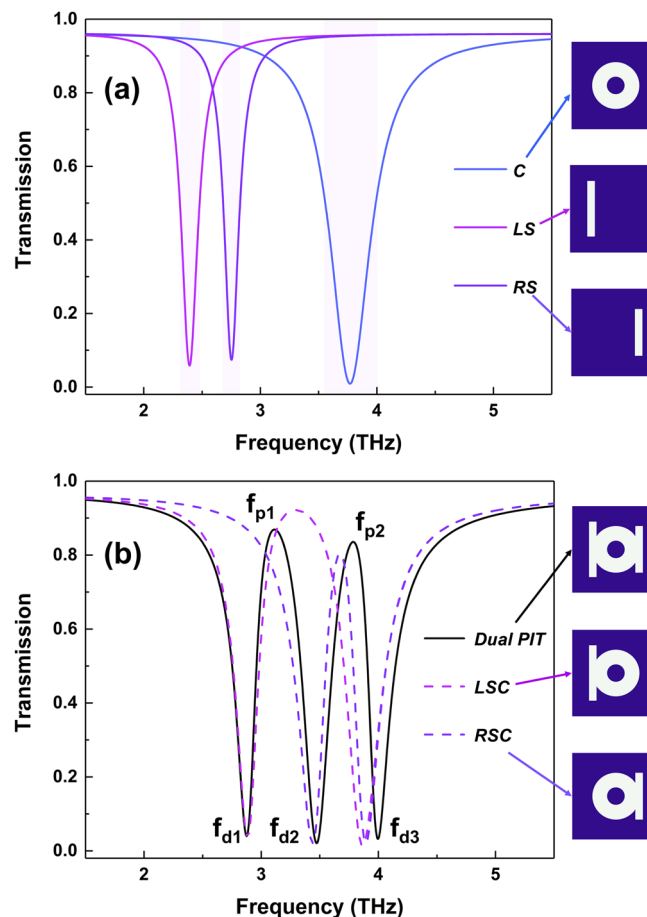
Fig. 2. Simulated transmission spectra of (a) sole *C* (blue solid line), sole *LS* (dark purple solid line), and sole *RS* (bright purple solid line) metamaterial structures; (b) the proposed metamaterial (black solid line), sole *LSC* (dark purple dashed line), and sole *RSC* (bright purple dashed line) metamaterial structures. The illustrations represent one-unit cell of each structure. The parameters of graphene are $E_F = 1.2$ eV and $\mu = 3.0\mu_c$.

different from dark modes, which do not couple to the incident field. In addition, the coupling of the *LS* structure (first quasi-dark mode) to the incident field is stronger than the one of the *RS* structure (second quasi-dark mode). When the *LS* and *RS* structures are combined with the *C* structure to form the *LSC* and *RSC* structures, respectively, these structures exhibit single PIT responses [dark purple dashed line and bright purple dashed line in Fig. 2(b)]. Finally, when the *C*, *LS*, and *RS* structures are combined into the composite proposed metamaterial, there are two transparency windows in the transmission spectra [black solid line in Fig. 2(b)], i.e. we have a dual PIT response. Since the three elements of the metamaterial have different resonant frequencies [Fig. 2(a)], the two transparency windows of the dual PIT response exhibit asymmetry in frequency. It is worth noting that transmission spectra with asymmetric transparency windows have sharper spectral profile compared to spectra with symmetric transparency windows, which can lead to higher sensitivity [46].

The large overlap between the left graphene strip and the graphene ring as well as between the right graphene strip and the graphene ring significantly affect the modes of the proposed metamaterial structure. The resonant frequency of the mode of the sole left strip structure is 2.39 THz [Fig. 2(a)]. The resonant frequency of the mode of the proposed metamaterial structure which is mostly localized on the left strip is 2.88 THz [Fig. 2(b)]. This large shift in the resonant frequency is due to the large overlap between the left strip and the ring in the proposed structure. Similarly, the resonant frequencies of the modes of the sole right strip structure and of the proposed metamaterial structure which is mostly localized on the right strip are 2.75 THz [Fig. 2(a)] and 3.45 THz [Fig. 2(b)], respectively. Again, a large shift is observed due to the large overlap between the right strip and the ring in the proposed structure. Finally, the resonant frequencies of the modes of the sole ring structure and of the proposed metamaterial structure which is mostly localized on the ring are 3.76 THz [Fig. 2(a)] and 3.99 THz [Fig. 2(b)], respectively. In this case the overlap between the ring and the strips results in a smaller shift of the resonant frequency. We note that we chose to have overlap between the *C* and *LS* and *C* and *RS* structures in the proposed metamaterial because this leads to superior sensing performance.

We also note that the mode of the proposed metamaterial structure which is mostly localized on the left strip is affected by the left strip-ring overlap. On the other hand, by comparing the transmission spectra of the *LSC* and proposed metamaterial structures [Fig. 2(b)], we conclude that the right strip-ring overlap does not significantly affect this mode. Similarly, the mode of the proposed metamaterial structure which is mostly localized on the right strip is affected by the right strip-ring overlap, while the left strip-ring overlap does not significantly affect this mode.

To better understand the physical mechanism behind the dual PIT behavior, we show the z-component of electric field (E_z) distributions in the proposed dual PIT metamaterial structure at the transmission dips at $f_{d1} = 2.88$ THz, $f_{d2} = 3.45$ THz, and $f_{d3} = 3.99$ THz in Figs. 3(a), 3(b), and 3(c), respectively. We also show the distributions at the transmission peaks at $f_{p1} = 3.11$ THz and $f_{p2} = 3.77$ THz in Figs. 3(d) and 3(e), respectively. In Figs. 3(a), 3(b), and 3(c) we observe that the electric field is mostly localized around the edges of the *LS*, *RS*, and *C* structures, respectively, similar to the electric field of optical dipole antennas. Thus, the three dips are caused by the direct coupling between each of these three modes and the incident light. In contrast to the E_z distributions at the transmission dips [Figs. 3(a), 3(b), and 3(c)], the E_z distributions at the transmission peaks [Figs. 3(d) and 3(e)] are not localized and extend over the whole structure. We attribute these distributions to the interference between the two quasi-dark modes and the bright mode supported by the structure.

3.2.   Theoretical analysis

The three modes mentioned above as well as the incident light can be considered as photon states [47]. The incident light can be assumed to be the ground (continuum) state $|0\rangle$. The excited states of the bright mode *C*, the first quasi-dark mode *LS*, and the second quasi-dark mode
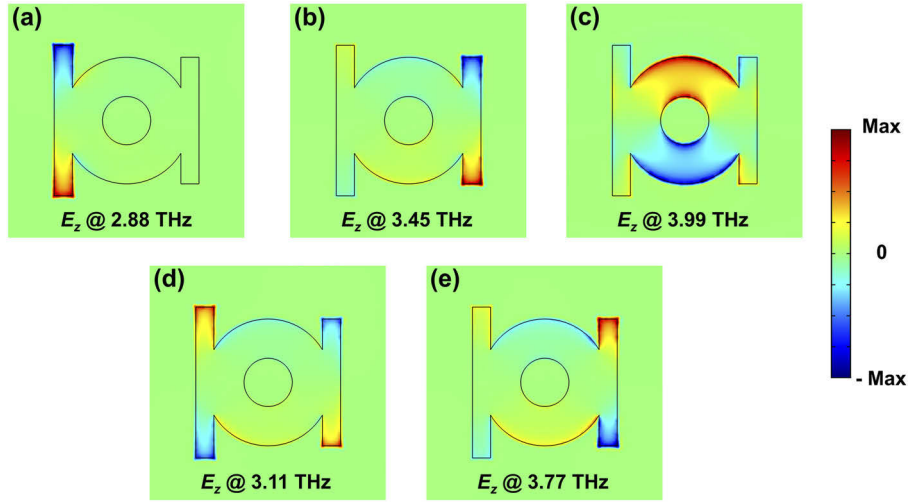
Fig. 3. The z-component of electric field (E_z) distributions in the proposed dual PIT metamaterial structure at (a) $f_{d1} = 2.88$ THz, (b) $f_{d2} = 3.45$ THz, (c) $f_{d3} = 3.99$ THz, (d) $f_{p1} = 3.11$ THz, and (e) $f_{p2} = 3.77$ THz.

RS, which can be directly excited by the incident light, are assumed to be $|M_1\rangle = \tilde{M}_1(\omega)e^{i\omega t}$, $|M_2\rangle = \tilde{M}_2(\omega)e^{i\omega t}$, and $|M_3\rangle = \tilde{M}_3(\omega)e^{i\omega t}$, respectively. The external electromagnetic field is $\tilde{E}_0 e^{i\omega t}$. Based on the classical atomic system of EIT, here we propose a four-level plasmonic system as shown in Fig. 4 to model the hybridization coupling effect and destructive interference between these three modes in the proposed metamaterial.
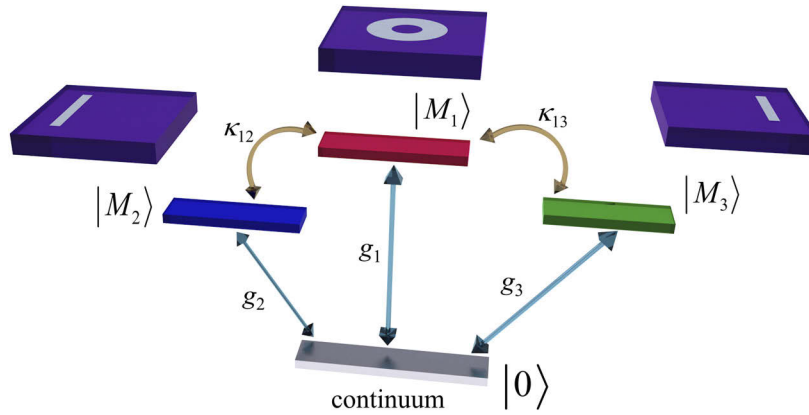
Fig. 4. Schematic diagram of the four-level plasmonic system for dual PIT.

Linearly coupled Lorentzian oscillators in the frequency domain are employed to describe the destructive interference. The field amplitudes can be obtained by [13,48–50]

$$
\begin{pmatrix}
\omega - \omega_{m1} + i\gamma_{m1} & \kappa_{12} & \kappa_{13} \\
\kappa_{12} & \omega - \omega_{m2} + i\gamma_{m2} & 0 \\
\kappa_{13} & 0 & \omega - \omega_{m3} + i\gamma_{m3}
\end{pmatrix}
\begin{pmatrix}
\tilde{M}_1 \\
\tilde{M}_2 \\
\tilde{M}_3
\end{pmatrix}
= -
\begin{pmatrix}
g_1 \tilde{E}_0 \\
g_2 \tilde{E}_0 \\
g_3 \tilde{E}_0
\end{pmatrix},
\quad (3)
$$

where ω is the angular frequency of the incident light, and ω_{mi} and γ_{mi} (i=1, 2, 3) represent the resonant angular frequencies and damping factors of the bright mode, the first quasi-dark mode, and the second quasi-dark mode, respectively. In addition, κ_{12} and κ_{13} are the parameters describing the coupling strength between $|M_1\rangle$ and $|M_2\rangle$, and $|M_1\rangle$ and $|M_3\rangle$, respectively. Finally, g_1, g_2, and g_3 are geometric parameters indicating how strongly the *C*, *LS*, and *RS* structures couple with the incident light.

In Eq. (3), the complex amplitude of the bright mode $\tilde{M}_1$ is proportional to the polarizability of the plasmonic system [13,48]. Thus, the normalized energy dissipation as a function of frequency can be derived as

$$P(\omega) = \left|\frac{\tilde{M}_1}{\tilde{E}_0}\right|^2 = \left|\frac{-g_1 + \frac{g_2\kappa_{12}}{(\omega-\omega_{m2}+i\gamma_{m2})} + \frac{g_3\kappa_{13}}{(\omega-\omega_{m3}+i\gamma_{m3})}}{(\omega - \omega_{m1} + i\gamma_{m1}) - \frac{\kappa_{12}^2}{(\omega-\omega_{m2}+i\gamma_{m2})} - \frac{\kappa_{13}^2}{(\omega-\omega_{m3}+i\gamma_{m3})}}\right|^2. \tag{4}$$

The transmission coefficient can then be obtained by

$$T(\omega) = 1 - P(\omega). \tag{5}$$

As we mentioned above, the destructive interference between the two quasi-dark modes and the bright mode induces the dual PIT effect. However, based on the proposed four-level plasmonic system, we can draw a further conclusion that the destructive interference of three pathways ($|0\rangle \rightarrow |M_1\rangle$, $|0\rangle \rightarrow |M_1\rangle \rightarrow |M_2\rangle \rightarrow |M_1\rangle$, and $|0\rangle \rightarrow |M_1\rangle \rightarrow |M_3\rangle \rightarrow |M_1\rangle$) results in the dual PIT effect.

In addition to the linearly coupled Lorentzian oscillators model used here [13,48–50], coupled-mode theory (CMT) can also be used to analyze the underlying physics of PIT [26,51–53].

4. Discussion

4.1. Sensing performance of the proposed metamaterial

In terms of sensing performance, dual PIT windows are very sensitive to the changes in the surrounding medium. One potential application is therefore sensing in the THz range. Thus, we study the sensing properties of the proposed metamaterial by varying the refractive index of the surrounding medium above the structure, as shown in Fig. 5(a). As before, the refractive index of the dielectric substrate is 1.5 and the incident light is normally incident on the surface of the structure. Figure 5(b) shows the transmission spectra corresponding to the dual PIT effect as a function of the refractive index of the surrounding medium. The refractive index range considered includes the refractive indices of many important materials for THz sensing. We observe that the transmission spectra exhibit a red shift with the increase of the refractive index. If we assume that one side of the graphene layer is exposed to the surrounding medium with relative permittivity ε_1, and that the relative permittivity of the substrate is ε_2, the plasmon frequencies of graphene can be written as [54]

$$f = \frac{e}{\hbar}\sqrt{\frac{LE_F}{2\pi^3(\varepsilon_1 + \varepsilon_2)D}} - \frac{i}{4\pi\tau}, \tag{6}$$

where D is the outer graphene ring diameter, L is a dimensionless parameter which depends on the ratio of inner and outer diameters of the graphene ring, and the imaginary part accounts for the carrier relaxation lifetime. Based on Eq. (6), we can conclude that the resonant frequency decreases as the refractive index ($n = \sqrt{\varepsilon_1}$) increases. This leads to a red shift.

In addition, we plot the frequency shifts of peak 1 and peak 2 relative to the refractive index in Fig. 5(c). We observe a linear increase in frequency shift with the refractive index. Thus, we demonstrate that the proposed structure has a potential application in sensing. The refractive
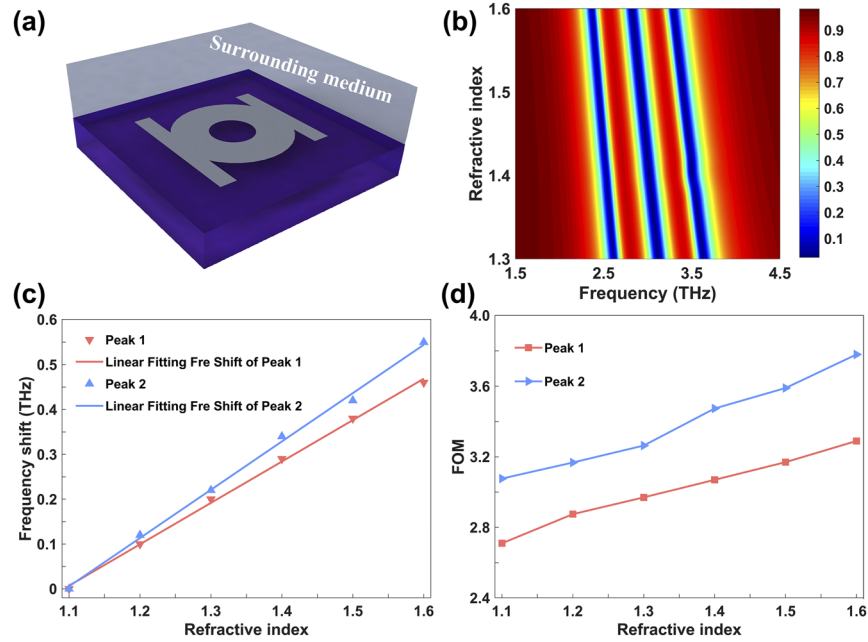
Fig. 5. (a) The sensing model of the metamaterial. (b) The evolution of the transmission spectra for different refractive index. (c) Frequency shifts of peak 1 and peak 2 versus the refractive index. (d) The value of *FOM* versus the refractive index.

index sensitivity *S*, which is defined as the ratio of the variation of the transmission peak position to the refractive index unit ($S = \Delta f / \Delta n$), can be used to evaluate the sensing performance of the structure. Using Fig. 5(c), we calculate high refractive index sensitivities of $S_1 = 0.92$ THz/RIU and $S_2 = 1.08$ THz/RIU. Here, S_1 and S_2 represent the sensitivities of transmission peaks 1 and 2, respectively. Both of these values are much higher compared to previously reported results in the THz region [55–58]. The sensitivities of the structures mentioned above are compared with our structure in Table 1. If we convert these numbers into $\Delta\lambda$/RIU by using $|\Delta\lambda / \Delta n| = (c / f_0^2) \times S$, where *c* is the speed of light in vacuum and f_0 represents the frequency of the transmission peak position, we obtain 28720 nm/RIU and 22917 nm/RIU, which are four to five times higher compared to 6750 nm/RIU in Ref. [55], and 5189 nm/RIU in Ref. [59].

**Table 1. Comparison of the proposed structure with previously reported structures.**

Sensor	Sensitivity
Ref. [55]	$S = 0.36$ THz/RIU
Ref. [56]	$S = 0.53$ THz/RIU
Ref. [57]	$S = 0.44$ THz/RIU
Ref. [58]	$S = 0.59$ THz/RIU
Proposed structure	$S_1 = 0.92$ THz/RIU, $S_2 = 1.08$ THz/RIU

In addition, the sensing performance can also be quantified by using the figure of merit (*FOM*) which is defined as

$$FOM = \frac{S(THz/RIU)}{FWHM(THz)}, \tag{7}$$

where *S* is the sensitivity. Figure 5(d) shows the *FOM* of the two transmission peaks as a function of the refractive index. When the refractive index is equal to 1.6, FOM_1 and FOM_2 are equal to ~3.29 and ~3.78, respectively.

In addition to silica, several other materials are used as substrate to make metamaterials applicable in different fields for refractive index sensing. For example, some low-loss semiconductors (such as silicon, GaAs, etc.) and polymers (such as PTFE, polyimide, PTE, etc.) are also used as substrate. However, the sensing performance can be influenced by the substrate since the relative permittivity of the substrate may affect the effective permittivity of the metamaterial. We therefore investigate the sensing performance of the proposed metamaterial with different substrate materials: PTFE (n=1.43), polyimide (n=1.79), and silicon (n=3.45). Figure 6 shows the transmission spectra around the positions of peak 1 and peak 2 for PTFE, SiO_2, and polyimide substrates. The sensitivity of the metamaterial for all substrate materials considered, including silicon, is shown in Figs. 7 and 8. The refractive index of the surrounding medium is set equal to 1.4. The transmission spectra exhibit a red shift when the refractive index of the substrate increases, which is consistent with Eq. (6).
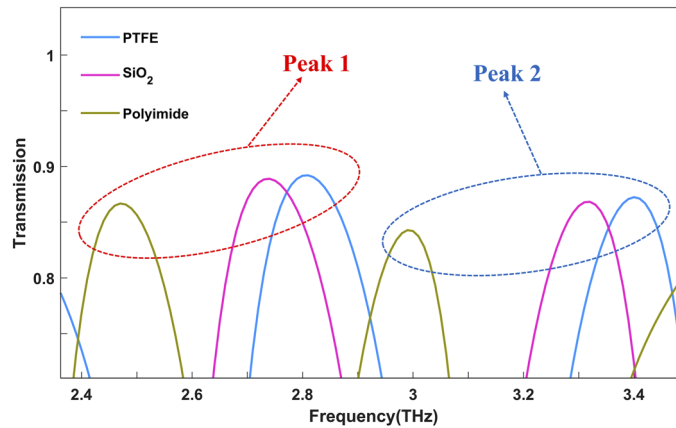

Fig. 6. Transmission spectra around peak 1 and peak 2 for different substrates.
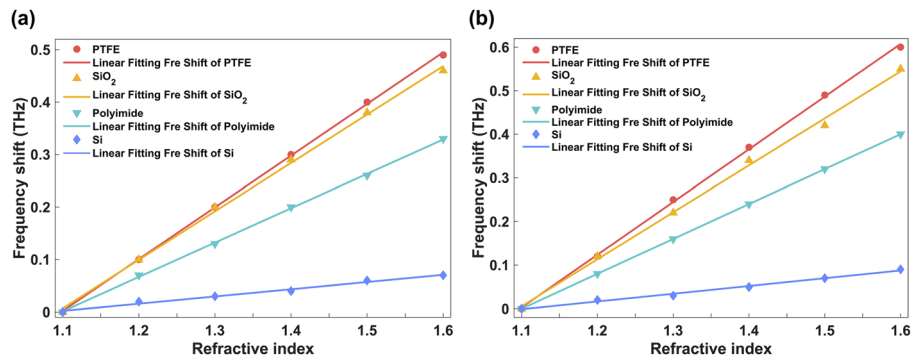
Fig. 7. Frequency shifts of (a) peak 1 and (b) peak 2 versus the refractive index of the surrounding medium for different substrate materials.

Figure 7 depicts the frequency shifts of peak 1 and peak 2 versus the refractive index of the surrounding medium for different substrate materials. For all kinds of substrates, the frequency shifts for both peak 1 and peak 2 increase linearly with the increase of refractive index of
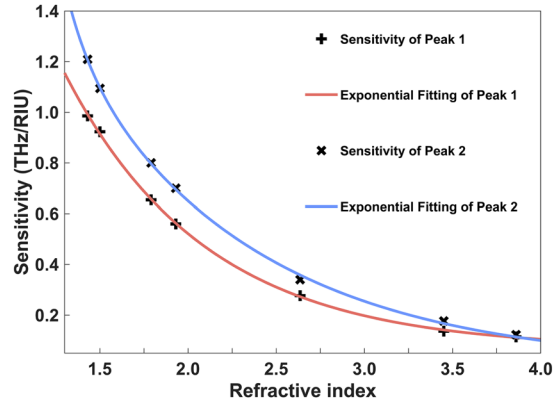
Fig. 8. The relationship between the sensitivities and the refractive index of the substrate.

the surrounding medium. Using the results of Fig. 7, we can calculate the sensitivities of the metamaterial for different substrates, as shown in Fig. 8. We observe that the sensitivity decays exponentially with the refractive index (Fig. 8). For example, when we choose silicon (n=3.45) as the substrate, the sensitivities of peak 1 and peak 2 are 0.14 THz/RIU and 0.18 THz/RIU, respectively. Thus, a substrate with large refractive index greatly degrades the sensing performance of the metamaterial.

Based on the results presented here, we can conclude that the proposed structure has great potential as a multi-frequency refractive index sensor in the terahertz region. In addition, we found that increasing the refractive index of the substrate leads to decreased sensitivity.

4.2. Tunability of the dual PIT

Based on the discussion above, one of the advantages of graphene-based metamaterials is that the surface plasmon resonant frequencies can be dynamically tuned by adjusting the Fermi energy of the graphene layer without having to modify the device geometry. Figure 9(a) shows numerical simulations (blue asterisks) and theoretical calculations (red solid line) of the dual PIT effect. We observe that the theoretical results are in good agreement with the FEM simulation results, which demonstrates the validity of the proposed four-level plasmonic system model. In addition, in Fig. 9(a) we observe that the transmission spectra exhibit a remarkable blue shift as the Fermi energy varies from 0.9 eV to 1.2 eV. This is consistent with [49]

$$f \propto \sqrt{\frac{\alpha_0 c E_F}{2\pi^2 \hbar L}} \propto \sqrt{E_F}, \tag{8}$$

where f is the resonant frequency of graphene, c is the speed of light, L represents the length of the graphene strip, and α_0 represents the fine structure constant. Based on Eq. (8), the resonant frequency increases as the Fermi energy increases.

Figure 9(b) shows ω_{m1}, ω_{m2}, and ω_{m3} as a function of the Fermi energy. We observe that the intrinsic resonant frequencies of the three modes increase linearly with the Fermi energy. The coupling coefficients (κ_{12} and κ_{13}) and damping factors (γ_{m1}, γ_{m2}, and γ_{m3}) play a key role in the transmission spectra. In Fig. 9(c) we therefore plot κ_{12}, κ_{13}, γ_{m1}, γ_{m2}, and γ_{m3} as a function of the Fermi energy. We observe that these parameters do not vary significantly with the Fermi energy. Thus, the variation in Fermi energy has almost no influence on the shape of the transmission spectra. The Fermi energy mostly affects the resonant frequencies, so that the metamaterial exhibits dual PIT behavior in a wide frequency range with weakly varying widths of the transparency windows. When the Fermi energy of graphene is equal to 1.2 eV,
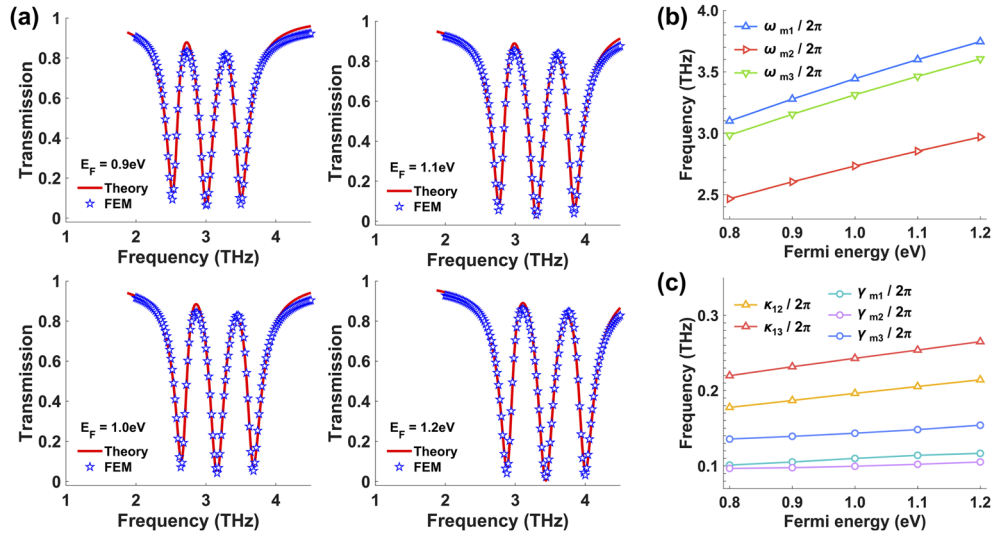
Fig. 9. (a) Transmission spectra calculated with FEM numerical simulations (blue asterisks) and theoretical calculations (red solid line) with E_F varying from 0.9 eV to 1.2 eV. (b-c) The fitting parameters in the four-level plasmonic system model as a function of the Fermi energy. Their values are extracted by fitting the simulated transmission spectra using the nonlinear least squares method of the MATLAB curve fitting toolbox.

the values of parameters $\gamma_{m1}/2\pi$, $\gamma_{m2}/2\pi$, $\gamma_{m3}/2\pi$, $\kappa_{12}/2\pi$, $\kappa_{13}/2\pi$, $g_1/2\pi$, $g_2/2\pi$, and $g_3/2\pi$ are 0.1167, 0.1053, 0.1539, 0.2143, 0.265, 0.3183, 0.2228, and 0.1592, respectively, in units of THz. Their values are extracted by fitting the simulated transmission spectra using the nonlinear least squares method of the MATLAB curve fitting toolbox.

The transmission dips and peaks of dual PIT as a function of the Fermi energy are shown in Fig. 10(a). We observe that the resonant frequencies linearly increase with the Fermi energy. In addition, the evolution of the transmission spectra as the Fermi energy is varied are shown in Fig. 10(b). We observe a blue shift in the spectra, as the Fermi energy increases. Using the tunability of graphene's Fermi energy, the proposed metamaterial can exhibit high sensitivities over a wide tunable range in the THz. This undoubtedly increases its application potential as a sensor.
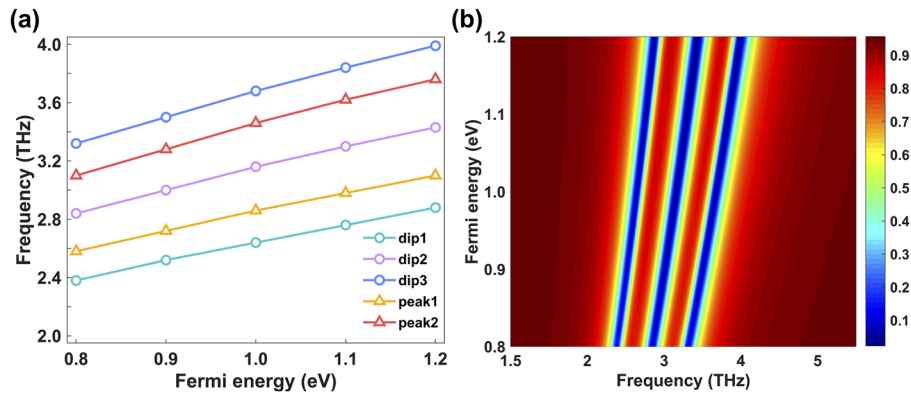
Fig. 10. (a) Resonant dips and peaks versus Fermi energy. (b) The evolution of the transmission spectra as a function of the Fermi energy.

The angle of incidence also plays a key role in tuning the response of the proposed structure. Here, we calculate the transmission spectra as a function of both frequency and angle of incidence, as shown in Figs. 11(a) and 11(b). We note that the angle of incidence has no influence on the positions of the resonant frequencies. This is due to the following reasons: first, the resonances in the *C*, *LS*, and *RS* structures are localized, and the LSPs at the graphene-dielectric interface are strongly confined. In addition, the plasmon wavelength is much smaller than the operating wavelength of the device [38]. In addition, we find that the transmittance of these dual PIT windows is still close to 70% when the incident angle exceeds 60°. This indicates that the proposed metamaterial is insensitive to incident angle variations, which is a desired feature for practical applications.
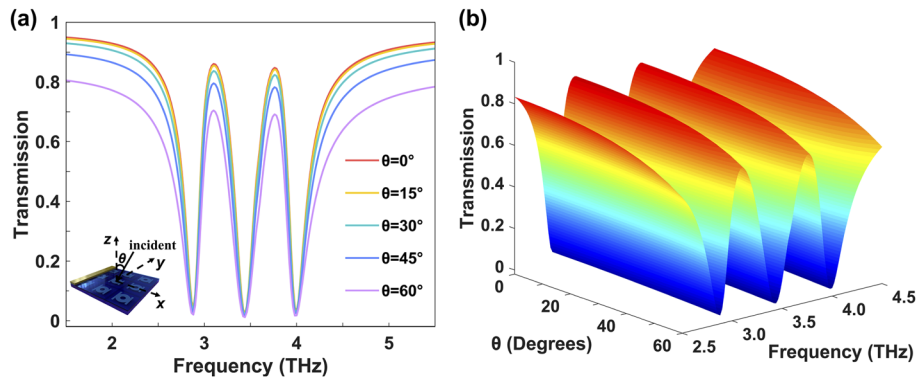
Fig. 11. Transmission spectra of the proposed structure for different angles of incidence θ. The plane of incidence is the *y-z* plane. The angle of incidence θ is shown in the inset. (b) The transmission spectra as a function of frequency and angle of incidence.

5. Conclusions

In summary, a monolayer graphene metamaterial is proposed to realize tunable dual PIT effect in the terahertz region. We propose a four-level plasmonic system model to comprehend the physical mechanism behind dual PIT, and the theoretical calculations agree well with the simulation results. Most importantly, the two transmission peaks can exhibit high refractive index sensitivities with 0.92 THz/RIU (28720 nm/RIU) and 1.08 THz/RIU (22917 nm/RIU). The influence of the refractive index of the substrate on the sensitivities is also studied in detail. Furthermore, the dual PIT effect can be effectively tuned by changing the Fermi energy of graphene and the angle of incidence. We show that the dual PIT effect persists until the incident angle exceeds 60°. Thus, the proposed graphene-based metamaterial may pave a new way for designing modulators, switches and multi-band refractive index sensors in the terahertz region.

Funding

Disclosures

The authors declare that there are no conflicts of interest related to this article.

References

1. X. Wu, M. Yun, M. Wang, C. Liu, K. Li, X. Qin, W. Kong, and L. Dong, "Self-imaging in multi-walled carbon nanotube arrays at visible wavelengths," Carbon **108**, 47–51 (2016).
2. K. Li, F. Xia, M. Wang, P. Sun, T. Liu, W. Hu, W. Kong, M. Yun, and L. Dong, "Discrete Talbot effect in dielectric graphene plasmonic waveguide arrays," Carbon **118**, 192–199 (2017).
3. S. Wang, P. K. Ang, Z. Wang, A. L. L. Tang, J. T. L. Thong, and K. P. Loh, "High Mobility, Printable, and Solution-Processed Graphene Electronics," Nano Lett. **10**(1), 92–98 (2010).
4. S. Kim, J. Nah, I. Jo, D. Shahrjerdi, L. Colombo, Z. Yao, E. Tutuc, and S. K. Banerjee, "Realization of a high mobility dual-gated graphene field-effect transistor with Al2O3 dielectric," Appl. Phys. Lett. **94**(6), 062107 (2009).
5. A. Vakil and N. Engheta, "Transformation Optics Using Graphene," Science **332**(6035), 1291–1294 (2011).
6. Y. Zhang, V. W. Brar, F. Wang, C. Girit, Y. Yayon, M. Panlasigui, A. Zettl, and M. F. Crommie, "Giant phonon-induced conductance in scanning tunnelling spectroscopy of gate-tunable graphene," Nat. Phys. **4**(8), 627–630 (2008).
7. F. Wang, Y. Zhang, C. Tian, C. Girit, A. Zettl, M. Crommie, and Y. R. Shen, "Gate-Variable Optical Transitions in Graphene," Science **320**(5873), 206–209 (2008).
8. S. H. Lee, M. Choi, T.-T. Kim, S. Lee, M. Liu, X. Yin, H. K. Choi, S. S. Lee, C.-G. Choi, S.-Y. Choi, X. Zhang, and B. Min, "Switching terahertz waves with gate-controlled active graphene metamaterials," Nat. Mater. **11**(11), 936–941 (2012).
9. L. Ju, B. Geng, J. Horng, C. Girit, M. Martin, Z. Hao, H. A. Bechtel, X. Liang, A. Zettl, Y. R. Shen, and F. Wang, "Graphene plasmonics for tunable terahertz metamaterials," Nat. Nanotechnol. **6**(10), 630–634 (2011).
10. T. Low and P. Avouris, "Graphene Plasmonics for Terahertz to Mid-Infrared Applications," ACS Nano **8**(2), 1086–1101 (2014).
11. F. H. L. Koppens, D. E. Chang, and F. J. G. de Abajo, "Graphene Plasmonics: A Platform for Strong Light–Matter Interactions," Nano Lett. **11**(8), 3370–3377 (2011).
12. C. You, A. C. Nellikka, I. D. Leon, and O. S. Magaña-Loaiza, "Multiparticle quantum plasmonics," Nanophotonics **9**(6), 1243–1269 (2020).
13. S. Zhang, D. A. Genov, Y. Wang, M. Liu, and X. Zhang, "Plasmon-Induced Transparency in Metamaterials," Phys. Rev. Lett. **101**(4), 047401 (2008).
14. S. E. Harris, "Electromagnetically Induced Transparency," Phys. Today **50**(7), 36–42 (1997).
15. K.-J. Boller, A. Imamoğlu, and S. E. Harris, "Observation of electromagnetically induced transparency," Phys. Rev. Lett. **66**(20), 2593–2596 (1991).
16. T.-T. Kim, H.-D. Kim, R. Zhao, S. S. Oh, T. Ha, D. S. Chung, Y. H. Lee, B. Min, and S. Zhang, "Electrically Tunable Slow Light Using Graphene Metamaterials," ACS Photonics **5**(5), 1800–1807 (2018).
17. A. Artar, A. A. Yanik, and H. Altug, "Multispectral Plasmon Induced Transparency in Coupled Meta-Atoms," Nano Lett. **11**(4), 1685–1689 (2011).
18. N. Liu, L. Langguth, T. Weiss, J. Kästel, M. Fleischhauer, T. Pfau, and H. Giessen, "Plasmonic analogue of electromagnetically induced transparency at the Drude damping limit," Nat. Mater. **8**(9), 758–762 (2009).
19. J. Wang, B. Yuan, C. Fan, J. He, P. Ding, Q. Xue, and E. Liang, "A novel planar metamaterial design for electromagnetically induced transparency and slow light," Opt. Express **21**(21), 25159–25166 (2013).
20. R. Yahiaoui, J. A. Burrow, S. M. Mekonen, A. Sarangan, J. Mathews, I. Agha, and T. A. Searles, "Electromagnetically induced transparency control in terahertz metasurfaces based on bright-bright mode coupling," Phys. Rev. B **97**(15), 155403 (2018).
21. S. khazaee and N. Granpayeh, "Tunable multiple plasmon induced transparencies in parallel graphene sheets and its applications," Opt. Commun. **406**, 199–204 (2018).
22. C. Zeng, Y. Cui, and X. Liu, "Tunable multiple phase-coupled plasmon-induced transparencies in graphene metamaterials," Opt. Express **23**(1), 545–551 (2015).
23. X. Chen and W. Fan, "Polarization-insensitive tunable multiple electromagnetically induced transparencies analogue in terahertz graphene metamaterial," Opt. Mater. Express **6**(8), 2607–2615 (2016).
24. H. Xu, H. Li, Z. He, Z. Chen, M. Zheng, and M. Zhao, "Dual tunable plasmon-induced transparency based on silicon–air grating coupled graphene structure in terahertz metamaterial," Opt. Express **25**(17), 20780–20790 (2017).
25. C. Sun, Z. Dong, J. Si, and X. Deng, "Independently tunable dual-band plasmonically induced transparency based on hybrid metal-graphene metamaterials at mid-infrared frequencies," Opt. Express **25**(2), 1242–1250 (2017).
26. E. Gao, Z. Liu, H. Li, H. Xu, Z. Zhang, X. Luo, C. Xiong, C. Liu, B. Zhang, and F. Zhou, "Dynamically tunable dual plasmon-induced transparency and absorption based on a single-layer patterned graphene metamaterial," Opt. Express **27**(10), 13884–13894 (2019).
27. H. Xu, M. Zhao, M. Zheng, C. Xiong, B. Zhang, Y. Peng, and H. Li, "Dual plasmon-induced transparency and slow light effect in monolayer graphene structure with rectangular defects," J. Phys. D: Appl. Phys. **52**(2), 025104 (2019).
28. W. Jia, P. Ren, Y. Jia, and C. Fan, "Active Control and Large Group Delay in Graphene-Based Terahertz Metamaterials," J. Phys. Chem. C **123**(30), 18560–18564 (2019).
29. Y. Cheng, K. Zhang, Y. Liu, S. Li, and W. Kong, "Actively mode tunable electromagnetically induced transparency in a polarization-dependent terahertz metamaterial," AIP Adv. **10**(4), 045026 (2020).
30. M. Liu, X. Yin, E. Ulin-Avila, B. Geng, T. Zentgraf, L. Ju, F. Wang, and X. Zhang, "A graphene-based broadband optical modulator," Nature **474**(7349), 64–67 (2011).

31. S. Xiao, T. Wang, T. Liu, X. Yan, Z. Li, and C. Xu, "Active modulation of electromagnetically induced transparency analogue in terahertz hybrid metal-graphene metamaterials," Carbon **126**, 271–278 (2018).

32. W. Pan, Y. Yan, Y. Ma, and D. Shen, "A terahertz metamaterial based on electromagnetically induced transparency effect and its sensing performance," Opt. Commun. **431**, 115–119 (2019).

33. C. Liu, P. Liu, L. Bian, Q. Zhou, G. Li, and H. Liu, "Dynamically tunable electromagnetically induced transparency analogy in terahertz metamaterial," Opt. Commun. **410**, 17–24 (2018).

34. V. Thareja, J.-H. Kang, H. Yuan, K. M. Milaninia, H. Y. Hwang, Y. Cui, P. G. Kik, and M. L. Brongersma, "Electrically Tunable Coherent Optical Absorption in Graphene with Ion Gel," Nano Lett. **15**(3), 1570–1576 (2015).

35. Z. Fang, Y. Wang, A. E. Schlather, Z. Liu, P. M. Ajayan, F. J. G. de Abajo, P. Nordlander, X. Zhu, and N. J. Halas, "Active Tunable Absorption Enhancement with Graphene Nanodisk Arrays," Nano Lett. **14**(1), 299–304 (2014).

36. S. Balci, O. Balci, N. Kakenov, F. B. Atar, and C. Kocabas, "Dynamic tuning of plasmon resonance in the visible using graphene," Opt. Lett. **41**(6), 1241–1244 (2016).

37. N. Mou, S. Sun, H. Dong, S. Dong, Q. He, L. Zhou, and L. Zhang, "Hybridization-induced broadband terahertz wave absorption with graphene metasurfaces," Opt. Express **26**(9), 11728–11736 (2018).

38. J. Zhang, Z. Zhu, W. Liu, X. Yuan, and S. Qin, "Towards photodetection with high efficiency and tunable spectral selectivity: graphene plasmonics for light trapping and absorption engineering," Nanoscale **7**(32), 13530–13536 (2015).

39. D. Wu, M. Wang, H. Feng, Z. Xu, Y. Liu, F. Xia, K. Zhang, W. Kong, L. Dong, and M. Yun, "Independently tunable perfect absorber based on the plasmonic properties in double-layer graphene," Carbon **155**, 618–623 (2019).

40. W. Du, K. Li, D. Wu, K. Jiao, L. Jiao, L. Liu, F. Xia, W. Kong, L. Dong, and M. Yun, "Electrically controllable directional coupler based on tunable hybrid graphene nanoplasmonic waveguide," Opt. Commun. **430**, 450–455 (2019).

41. J.-H. Chen, C. Jang, S. Xiao, M. Ishigami, and M. S. Fuhrer, "Intrinsic and extrinsic performance limits of graphene devices on SiO_2," Nat. Nanotechnol. **3**(4), 206–209 (2008).

42. M. S. Islam, J. Sultana, M. Biabanifard, Z. Vafapour, M. J. Nine, A. Dinovitser, C. M. B. Cordeiro, B. W.-H. Ng, and D. Abbott, "Tunable localized surface plasmon graphene metasurface for multiband superabsorption and terahertz sensing," Carbon **158**, 559–567 (2020).

43. K. Zhang, C. Wang, L. Qin, R.-W. Peng, D.-H. Xu, X. Xiong, and M. Wang, "Dual-mode electromagnetically induced transparency and slow light in a terahertz metamaterial," Opt. Lett. **39**(12), 3539–3542 (2014).

44. M. Manjappa, S.-Y. Chiam, L. Cong, A. A. Bettiol, W. Zhang, and R. Singh, "Tailoring the slow light behavior in terahertz metasurfaces," Appl. Phys. Lett. **106**(18), 181101 (2015).

45. R. Yahiaoui, M. Manjappa, Y. K. Srivastava, and R. Singh, "Active control and switching of broadband electromagnetically induced transparency in symmetric metadevices," Appl. Phys. Lett. **111**(2), 021101 (2017).

46. L. Zhu, F.-Y. Meng, J.-H. Fu, Q. Wu, and J. Hua, "Multi-band slow light metamaterial," Opt. Express **20**(4), 4494–4502 (2012).

47. Z. He, X. Ren, S. Bai, H. Li, D. Cao, and G. Li, "Λ-Type and V-Type Plasmon-Induced Transparency in Plasmonic Waveguide Systems," Plasmonics **13**(6), 2255–2259 (2018).

48. X. Duan, S. Chen, H. Yang, H. Cheng, J. Li, W. Liu, C. Gu, and J. Tian, "Polarization-insensitive and wide-angle plasmonically induced transparency by planar metamaterials," Appl. Phys. Lett. **101**(14), 143105 (2012).

49. H. Cheng, S. Chen, P. Yu, X. Duan, B. Xie, and J. Tian, "Dynamically tunable plasmonically induced transparency in periodically patterned graphene nanostrips," Appl. Phys. Lett. **103**(20), 203112 (2013).

50. X. Duan, S. Chen, H. Cheng, Z. Li, and J. Tian, "Dynamically tunable plasmonically induced transparency by planar hybrid metamaterial," Opt. Lett. **38**(4), 483–485 (2013).

51. Z. Liu, E. Gao, Z. Zhang, H. Li, H. Xu, X. Zhang, X. Luo, and F. Zhou, "Dual-Mode On-to-Off Modulation of Plasmon-Induced Transparency and Coupling Effect in Patterned Graphene-Based Terahertz Metasurface," Nanoscale Res. Lett. **15**(1), 1 (2020).

52. Z. Liu, X. Zhang, Z. Zhang, E. Gao, F. Zhou, H. Li, and X. Luo, "Simultaneous switching at multiple frequencies and triple plasmon-induced transparency in multilayer patterned graphene-based terahertz metamaterial," New J. Phys. **22**(8), 083006 (2020).

53. Z. Liu, E. Gao, X. Zhang, H. Li, H. Xu, Z. Zhang, X. Luo, and F. Zhou, "Terahertz electro-optical multi-functional modulator and its coupling mechanisms based on upper-layer double graphene ribbons and lower-layer a graphene strip," New J. Phys. **22**(5), 053039 (2020).

54. Z. Fang, S. Thongrattanasiri, A. Schlather, Z. Liu, L. Ma, Y. Wang, P. M. Ajayan, P. Nordlander, N. J. Halas, and F. J. G. de Abajo, "Gated Tunability and Hybridization of Localized Plasmons in Nanostructured Graphene," ACS Nano **7**(3), 2388–2395 (2013).

55. P. Tang, J. Li, L. Du, Q. Liu, Q. Peng, J. Zhao, B. Zhu, Z. Li, and L. Zhu, "Ultrasensitive specific terahertz sensor based on tunable plasmon induced transparency of a graphene micro-ribbon array structure," Opt. Express **26**(23), 30655–30666 (2018).

56. S. Hu, D. Liu, H. Yang, H. Wang, and Y. Wang, "Staggered H-shaped metamaterial based on electromagnetically induced transparency effect and its refractive index sensing performance," Opt. Commun. **450**, 202–207 (2019).

57. C. Liu, P. Liu, C. Yang, Y. Lin, and S. Zha, "Dynamic electromagnetically induced transparency based on a metal-graphene hybrid metamaterial," Opt. Mater. Express **8**(5), 1132–1142 (2018).

58. H. Zhang, Y. Cao, Y. Liu, Y. Li, and Y. Zhang, "A novel graphene metamaterial design for tunable terahertz plasmon induced transparency by two bright mode coupling," Opt. Commun. **391**, 9–15 (2017).
59. Y. Zhang, T. Li, B. Zeng, H. Zhang, H. Lv, X. Huang, W. Zhang, and A. K. Azad, "A graphene based tunable terahertz sensor with double Fano resonances," Nanoscale **7**(29), 12682–12688 (2015).